Pumping mechanism of NM-R3, a light-driven bacterial chloride importer in the rhodopsin family

Ji-Hye Yun[1]*, Mio Ohki[2,3]*, Jae-Hyun Park[1], Naito Ishimoto[3], Ayana Sato-Tomita[4], Wonbin Lee[1], Zeyu Jin[1], Jeremy R. H. Tame[3], Naoya Shibayama[4], Sam-Yong Park[3†], Weontae Lee[1†]

A newly identified microbial rhodopsin, NM-R3, from the marine flavobacterium *Nonlabens marinus*, was recently shown to drive chloride ion uptake, extending our understanding of the diversity of mechanisms for biological energy conversion. To clarify the mechanism underlying its function, we characterized the crystal structures of NM-R3 in both the dark state and early intermediate photoexcited states produced by laser pulses of different intensities and temperatures. The displacement of chloride ions at five different locations in the model reflected the detailed anion-conduction pathway, and the activity-related key residues—Cys[105], Ser[60], Gln[224], and Phe[90]— were identified by mutation assays and spectroscopy. Comparisons with other proteins, including a closely related outward sodium ion pump, revealed key motifs and provided structural insights into light-driven ion transport across membranes by the NQ subfamily of rhodopsins. Unexpectedly, the response of the retinal in NM-R3 to photostimulation appears to be substantially different from that seen in bacteriorhodopsin.

INTRODUCTION

Rhodopsins are integral membrane proteins holding a retinal chromophore within a hydrophobic cavity, where they form a protonated Schiff base (PSB) with an essential lysine residue in the seventh (G) helix (Fig. 1A) (*1*). Light-induced isomerization of the chromophore allows these proteins to act as photosensors or light-driven pumps. The structures of bacteriorhodopsin (bR), which pumps protons out, and halorhodopsin (hR), which pumps chloride ions in, are established (*2–4*). Two representative structures of hRs from *Halobacterium salinarum* (HsHR) and *Natronomonas pharaonis* (NpHR) show common structural features, including a homotrimeric conformation with a large hydrophobic cap, formed by the extracellular loop between helices B and C, which covers most of the extracellular surface of the protein (*4*). The Schiff base linking the protein to the chromophore is protonated during the dark state when the receptor is at rest. In bR, the photocycle is initiated by the photoisomerization of the all-trans retinal (ATR), moving a proton from the Schiff base to the acceptor side chain of Asp[85] (*5*). The Schiff base is reprotonated by Asp[96], leading to proton pumping. These two aspartate residues, together with Thr[89], form a "DTD" (Asp, Thr, and Asp) motif in the C helix, which is characteristic of proton transporters in the rhodopsin family, although the threonine is not functionally required (*5*). In hR, a TSA (Thr, Ser, and Ala) motif replaces the DTD motif, and the specificity of the protein for either chloride ions or protons is strongly linked to whichever of the two motifs is present. The replacement of Asp[85] in bR with threonine yields a chloride-transporting mutant (*6, 7*).

A new subfamily called NQ (Asn and Gln) rhodopsins was first identified in 2000. NQ rhodopsins are found in marine bacteria and archaea, with Asn and Gln in place of the acceptor and donor aspartate

residues of bR, respectively. *Nonlabens marinus* rhodopsin-3 (NM-R3) is an inward chloride pump in the NQ rhodopsin subfamily (*7, 8*). It shares 35% sequence identity with *Krokinobacter eikastus* rhodopsin 2 (KR2), a light-driven sodium exporter (*9–13*). Two crystal structures of NM-R3 in the dark state have been published, and two chloride ions are found; Cl-1 lies close to the Schiff base, and Cl-2 lies in an extracellular surface pocket (*11, 12*). The network of bonds between chloride ions and highly ordered water molecules in NM-R3 is different from that of other chloride-pumping rhodopsins (*4, 14, 15*). Overlaying NM-R3 and NpHR with secondary-structure matching (SSM) (*16*) shows that the proteins share 17% sequence identity, and a core region of 202 Cα atoms gives a root mean square deviation (RMSD) of 1.79 Å. The lack of conservation among functionally important residues, such as Thr[218] of NpHR (*17*), equivalent to Met[197] in NM-R3, suggests that the mechanisms of these proteins are notably different. The B-C loop of NM-R3 reveals a different conformation than that in other rhodopsin subfamilies and includes three tyrosine residues (Tyr[76], Tyr[78], and Tyr[83]), which form part of a cluster of aromatic side chains on the extracellular face of the protein. Moreover, three nearby aromatic residues (Phe[15], Trp[72], and Tyr[83]) stack together to form the "3 omega motif," which is highly conserved among the NQ family of ion pumps but not found in bR or hR. Detailed spectroscopic studies of NM-R3 have suggested that the photocycle involves five or six distinct intermediates, as in bR (*18*).

Low-temperature trapping has been used to obtain a crystallographic model of an early intermediate in the bR photocycle (*19*). More recently, the x-ray free electron laser (XFEL) was used to obtain a time series of models in femtosecond to millisecond time scales (*20, 21*). Although the retinal-binding pocket is highly conserved, Asp[85] in bR is replaced with Asn[98] in NM-R3, which lies approximately 3 Å further from the retinal, creating the Cl-1 binding site, where a chloride ion can interact directly with the PSB. No other internal chloride ion binding sites have been suggested by spectroscopy (*22*). In the ground state of bR, Arg[82] lies 3.8 Å from Asp[212] (*23*); in NM-R3, the equivalent side chains of Arg[95] and Asp[231] form a hydrogen bond 2.7 Å long. NM-R3 also has Ser[234] in place of Ala[215], which forms a hydrogen bond with the conserved side chain of Tyr[204] alongside the chromophore, suggesting that the retinal-binding

[1]Department of Biochemistry, College of Life Science and Biotechnology, Yonsei University, Seoul 03722, South Korea. [2]Research Complex at Harwell, Rutherford Appleton Laboratory, OX11 0FA Didcot, UK. [3]Drug Design Laboratory, Graduate School of Medical Life Science, Yokohama City University, Tsurumi, Yokohama 230-0045, Japan. [4]Division of Biophysics, Department of Physiology, Jichi Medical University, 3311-1 Yakushiji, Shimotsuke, Tochigi 329-0498, Japan.
*These authors contributed equally to this work.
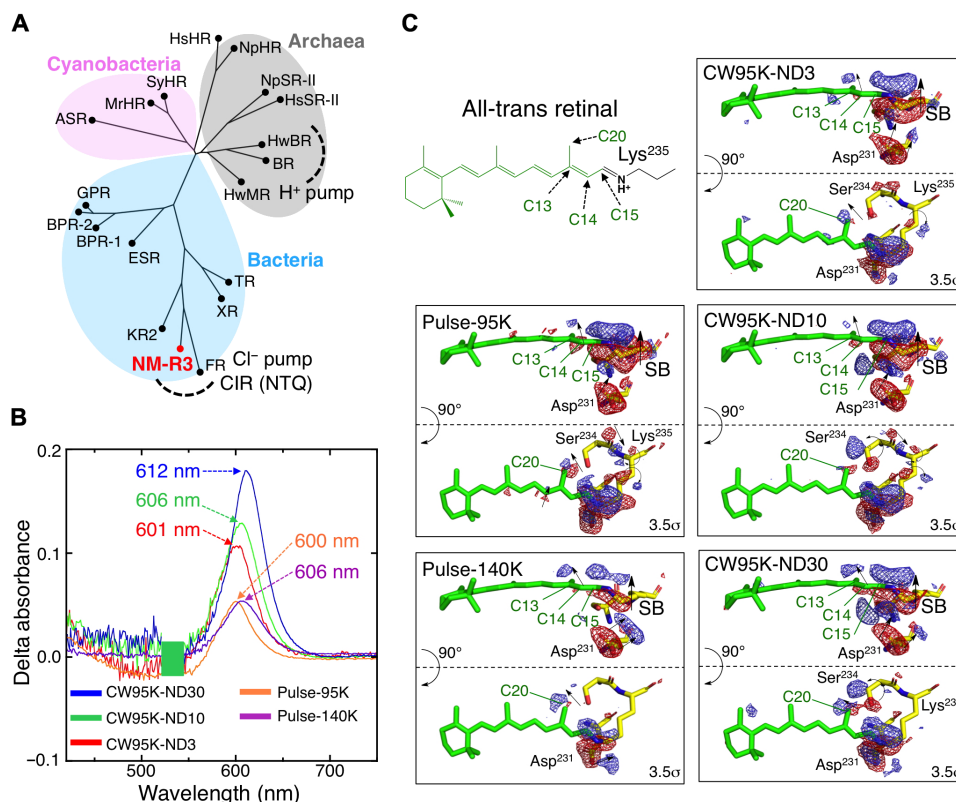†Corresponding author. Email: wlee@spin.yonsei.ac.kr (W.L.); park@yokohama-cu.ac.jp (S.-Y.P.)

Fig. 1. Structural characterization of NM-R3 retinal chromophores after light excitation. (**A**) Phylogenetic tree showing relationships among rhodopsins. (**B**) Difference absorption spectra showing the increasing red shift of the visible band near 600 nm with laser power. Spectra were obtained from the difference between the absorption spectra for the dark and light states, shown in fig. S1. (**C**) Difference electron density maps showing changes triggered near the retinal. $|F_{obs}|^{light} - |F_{obs}|^{dark}$ difference Fourier electron density maps contoured at ±3.5σ. Positive and negative values are shown in blue and red, respectively.

pocket of NM-R3 is substantially less flexible than that of bR. Since the light-induced structural changes and ion conduction pathway of NM-R3 remain much less well characterized than those of bR, we studied the photoexcitation of crystalline NM-R3, at different temperatures and using different excitation intensities, to elucidate the structural mechanism of the chloride pump and help understand the differences between the various ion pumps in the rhodopsin family.

RESULTS

Structural determination of early intermediate photoexcited states of NM-R3 by laser pulses of different intensities and temperatures

Using single-crystal microspectrophotometry, we exposed single crystals of NM-R3 at 95 K to light from a continuous wave (CW) green laser (532 nm) with 3% (CW95K-ND3), 10% (CW95K-ND10), or 30% (CW95K-ND30) neutral density (ND) filters; other crystals at 95 K (pulse-95K) or 140 K (pulse-140K) were irradiated with pulsed laser light. For each crystal, a stable light-induced red shift of the visible absorption band near 550 nm was observed, and the spectral changes increased as the laser intensity increased (Fig. 1B and fig. S1). The changes were rapid and fully reversible. Moreover, similar rate constants were observed for NM-R3 in solution, indicating that the crystal packing does not prevent rapid stimulation by light or reversion to the dark state. In both the crystal and solution conditions, accumulation and relaxation kinetics exhibited an initial overshoot and undershoot, respectively.

X-ray datasets were collected in the dark and after irradiation (Fig. 1C, fig. S2, and table S1). Comparing the 263 Cα atoms of residues 2 to 264, the highest RMSD between dark-state models was 0.074 Å. A comparison of the light- and dark-state models for each crystal revealed a maximum Cα RMSD of only 0.064 Å for CW95K-ND10, with a maximum displacement of 0.14 Å at Lys[119], at the protein surface and remote from crystal contacts. Even with the most intense photoexcitation (CW95K-ND30), the model showed small atomic shifts, and Cl-1 moved only by 0.2 Å. However, difference maps could be calculated with low background noise. The R-merge between the dark and photoexcited datasets was around 5% throughout, for every crystal, and showed no increase for images taken toward the end of data collection.

Similar to the spectra observed by microspectrophotometry with single crystals, electron density difference maps (light minus dark for each crystal) showed greater and more widespread changes with higher temperatures or laser intensities (Fig. 1C and fig. S3A). At 140 K, although changes were found throughout the protein, the local structural change near the retinal was smaller than that in CW95K-ND30, suggesting that photoexcitation effects had diffused throughout the entire structure. The temperature factors of the backbone were similar in all datasets and were unaffected by laser exposure (fig. S3B) so that features of the difference density maps obtained in this study cannot arise from simple thermal effects during the experiments.

Detailed structural differences of NM-R3 by photoexcitation

Figure 2 shows a close-up series of the difference density maps obtained with continuous laser excitation protocols, focusing on the
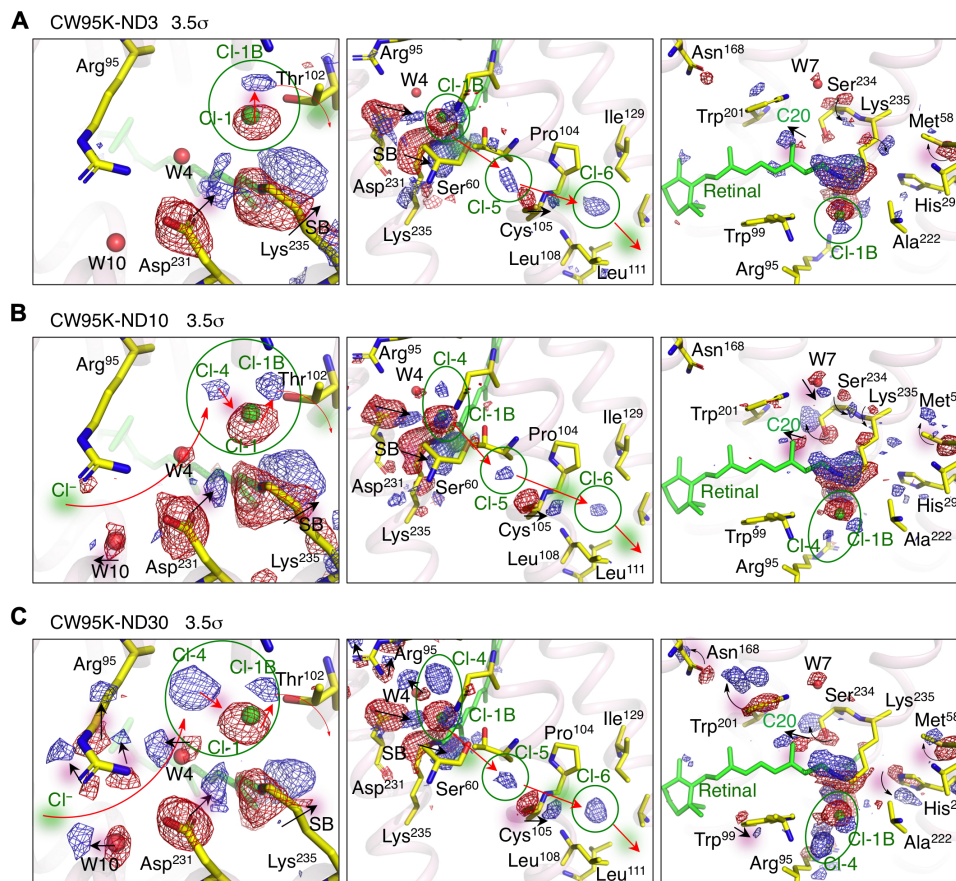
Fig. 2. Atomic movements induced by photoexcitation. $|F_{obs}|^{light} - |F_{obs}|^{dark}$ difference Fourier electron density map contoured at ±3.5σ in (**A**) CW95K-ND3, (**B**) CW95K-ND10, and (**C**) CW95K-ND30. For each map, three panels show different views of the retinal, and the central panel shows unexpected density peaks that appear consistently in each map. Red arrows suggest the movement of chloride ions following photoexcitation. Positive and negative values are shown in blue and red, respectively. The stick model represents the dark state of NM-R3. Additional views of the electron density maps are available in movies S1 and S2.

Schiff base and adjacent residues. Contoured at 5σ, the CW95K-ND3 difference map showed features close to the PSB, and a few other features appeared at 3.5σ (Fig. 2A). Positive and negative density indicated strongly concerted movements of the Schiff base, by about 0.2 Å, toward Thr[102] and away from Asp[231]. Strong density appears on either side of Nε and Cδ of the Lys[235] side-chain atoms but much less so for the retinal atoms. Despite the strong side-chain movement, the main-chain atoms of Lys[235] are unmoved. The retinal itself overlays closely with that of bR, with the exception of the C3 pucker, but there is no direct evidence for retinal isomerization in the NM-R3 electron density maps (at the level of excitation achieved). Unlike bR, no difference density is seen near the retinal C13═C14 bond (Fig. 1C and fig. S4). Paired positive and negative difference density features appear over the retinal C20 methyl group, which undergoes a structural shift comparable with that in bR, but the retinal maintains the all-trans conformation (21). Separate refinement of the model against data collected from the photoexcited crystal, and calculation of an $F_{light} - F_{dark}$ difference map using independent phases for the light and dark states, confirms that the largest structural changes at the chromophore are restricted to the lysine side chain and retinal C15, which form the Schiff base. The photoresponse of the retinal of NM-R3 in the early intermediate state is therefore markedly different from that of bR, both in which atoms move strongly and the direction of movement (21).

Several internal cavities (IC1 to IC3) have been identified in NM-R3 that contain water molecules and might help conduct chloride ions (12). IC1 holds Wat11 in our models, and IC3 holds Wat16, but neither water molecule is displaced in the difference maps. Wat4 forms hydrogen bonds with Trp[99], Arg[95], and Asp[231]. It is weakly disordered at lower excitation levels and showed slight movement toward Arg[95] in the CW95K-ND30 map (Fig. 2C). Wat10 and Wat37 were found within a pocket surrounded by Leu[21], Leu[22], Leu[65], Arg[95], Thr[228], and Asp[231]; both showed negative difference densities with photoexcitation, but the temperature factors (18 to 25 Å²) did not increase significantly. Water molecules do not therefore account for the strong positive density peaks that appear in hydrophobic pockets consistently across datasets (Fig. 2 and fig. S5), and these peaks may be interpreted as chloride movement from the extracellular to the cytoplasmic face of the protein.

Cl-1 is shifted away from the PSB toward Asn[98]. Negative density with no corresponding positive density is found at the side chain of Asp[231], indicating a loss of order rather than a directed movement. With increasing laser intensity and temperature, these changes increased, and features more distant from the chromophore became apparent (Fig. 2 and fig. S5). The side chains of Cys[55], Met[58], and Cys[105] become disordered, and Trp[201] (equivalent to Trp[182] in bR) becomes more mobile with stronger excitation. Contoured at 3.5σ, Ser[234] starts to flip the rotamer, breaking its hydrogen bond with Tyr[204]. Near the Cl-1 binding site, two positive difference electron

density peaks appear, indicating the outgoing chloride ion (Cl-1B) and incoming chloride ion (Cl-4), but only the first of these peaks is evident in the CW95K-ND3 map (Fig. 2A). The intensity of both peaks becomes much higher with stronger excitation (Fig. 2, B and C). Two additional positive difference density peaks are found further from the retinal and represent the positions of chloride ions Cl-5 and Cl-6. Cl-5 appears between Ser[60] and Cys[105], and Cl-6 appears on the far side of Cys[105], in a pocket formed with Ala[125] and Ile[129] (Fig. 2B). These features are found in all the maps, including pulse-95K and pulse-140K, with the Cl-6 position becoming especially strong in the CW95K-ND30 map (Fig. 2C).

Chloride conduction pathway of NM-R3

Contouring the difference electron density maps at 3.2σ shows a set of positive peaks within the body of the protein that apparently map out the migration path for substrate chloride ions moving from the extracellular face to the cytoplasmic face (Fig. 3). Additional views of the movement of the chloride ions are shown in fig. S4. In the dark state, chloride ion Cl-1 is found very close to the chromophore but lying toward the extracellular face. On photoexcitation, this chloride ion moves slightly to position Cl-1B, or further to the two positions (Cl-5 and Cl-6) near Cys[105], closer to the cytoplasmic face of the protein. An additional chloride ion, Cl-3, is found in a pocket near Phe[90], near the extracellular face. This peak of positive density appears most strongly in the CW95K-ND3 map and is reduced at higher temperature or laser power (Fig. 3). The position Cl-4 appears to indicate a chloride ion arriving near the PSB region from the extracellular face via Cl-3. In contrast to Cl-3, the height of this peak is significantly increased at higher laser power (Fig. 3 and Table 1).

Since the movements are so small, difference distance matrix plots are helpful to understand the overall structural changes (at the backbone level) of NM-R3 on photoexcitation (fig. S6). The changes seen in CW95K-ND30 and pulse-140K are very similar. Residues near the extracellular region (Ala[75] to Ala[77], Leu[85] to Leu[88] in the B-C loop, Ser[91] to Trp[99] in the C helix, and Thr[138] to Ser[160] in the D and E helices) move toward the interior of the protein. Residues near the cytoplasmic region (Leu[106] to Leu[116] in the C helix, Ile[49] to Thr[51] in the B helix, and Gln[249] to Ala[253] in the G helix) move outward (fig. S6).

Functional studies on residual mutants related to the chloride conduction pathway

Following the observation of density near internal residues, it was tested whether replacing these side chains might affect chloride transport activity. Pumping activity was greater for the C105A mutant than the wild type, while C105F exhibited weak activity, and S60F was nearly inactive. The Cl-3 site sits between Phe[90] and Gln[224]. Replacing either residue with tryptophan strongly reduced chloride transport, and the Q224W mutant was essentially inactive (Fig. 4). These results provide direct evidence that the residues identified by our crystallographic analysis have functional roles.

Ser[234], equivalent to an alanine in bR or *Hs*HR (figs. S7 and S8), is associated with color tuning and ion transport (*24, 25*). This serine is conserved in rhodopsins from cyanobacteria and marine bacteria but is replaced by asparagine or threonine in rhodopsin family members such as sensory rhodopsins. Mutation experiments showed that placing either of these residues at position 234 maintains NM-R3 activity and do not cause any red shift in the visible spectrum. The S234A mutant, however, has decreased activity, red shift of the principal visible absorption band, and weaker chloride ion binding (fig. S8). The discovery that Ser[234] breaks its hydrogen bond with Tyr[204] on photoexcitation (Fig. 2 and fig. S5) suggests that this residue may explain some of the differences in retinal conformation between bR and NM-R3 in early intermediate states.

DISCUSSION

Since its discovery almost 50 years ago, bR has been used as a model system, both as a protein fold and as a light-driven pump. Dozens of structural analyses have been reported, and numerous studies have attempted to relate the structural changes caused by photoexcitation to the directed transport of hydrogen ions (*26*). The large number of crystallographic structural models allows them to be clustered, showing clear grouping by crystallization conditions and space group, but this diversity of crystal forms has not prevented comparison of diffraction data from similar crystals in resting and excited states (*27*). By illuminating crystals at very low temperatures (100 or 110 K), several groups trapped
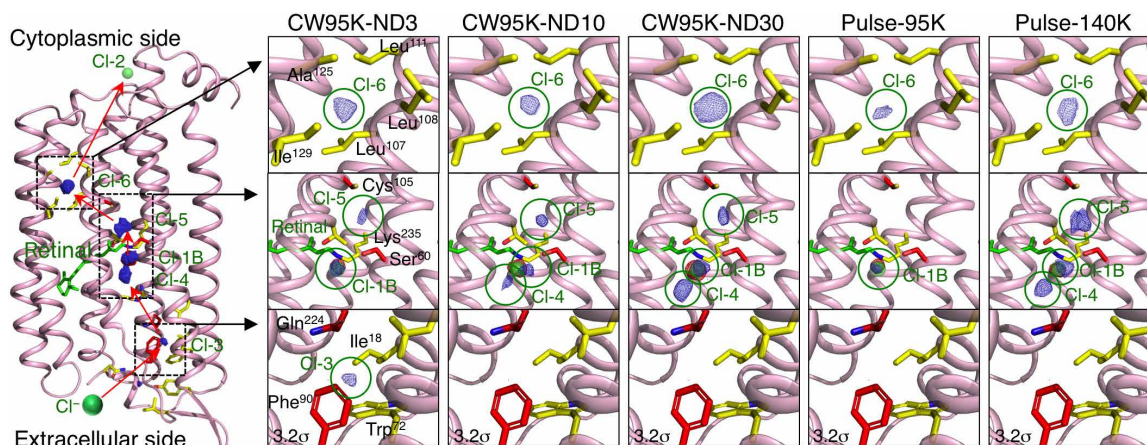

Fig. 3. Chloride ion conduction path from the extracellular to cytoplasmic face. $|F_{obs}|^{light} - |F_{obs}|^{dark}$ difference Fourier electron density maps contoured at ±3.2σ covering a ribbon diagram of the entire protein model. Residues surrounding each chloride ion are represented by stick models. Positive and negative values are shown in blue and red, respectively. Two chloride ions (Cl-1 and Cl-2) are present in the refined dark model, and four additional ions (Cl-3, Cl-4, Cl-5, and Cl-6) were identified from the difference density maps. The Cl-1 ion moves slightly to site Cl-1B. A chloride ion at the extracellular face, Cl-3, was observed only in CW95K-ND3.

Table 1. Summary of the intensity quantification of the difference Fourier electron density map for key water molecules, chloride ions, and residues. Values given in units of σ (equal to the root mean square electron density of the unit cell). Values below ±3.0σ were set to zero, as being of too low significance. Cells are colored according to the σ value, being darker green when the magnitude of the measured difference is stronger. Residue nomenclature: SC, side chain; BB, back bone; (+), positive density feature; (−), negative density feature.

Datasets	CW95K-ND3	CW95K-ND10	CW95K-ND30	Pulse-95K	Pulse-140K
S/D (e.A3/s)	0.006	0.012	0.016	0.009	0.016
Retinal					
C14/C15 (+)	5.4	7.6	6.9	9.3	6.1
C14/C15 (−)	−5.9	−7.0	−5.2	−9.2	−4.3
C20 (+)	4.3	3.9	4.4	4.9	4.8
C20 (−)	−3.5	−4.5	−5.4	−5.8	−4.2
Lys[235]					
Nz/CE (+)	11.0	9.8	8.5	10.9	4.9
Nz/CE (−)	−13.4	−16.8	−11.4	−15.3	−7.2
CD (+)	3.5	3.6	0.0	4.3	0.0
CD (−)	−7.1	−7.5	−3.8	−7.6	−3.8
CG (+)	0.0	3.8	3.15	4.7	0.0
CG (−)	0.0	−6.0	0.0	−6.6	0.0
BB (+)	3.3	4.5	0.0	4.6	0.0
BB (−)	−4.1	−4.7	−3.4	−4.5	−4.5
Ser[234]					
SC (+)	3.0	7.1	7.1	3.5	3.6
SC (−)	−4.2	−6.6	−6.0	−4.1	−3.6
BB (+)	3.7	4.5	3.4	4.8	3.0
BB (−)	−4.4	−4.8	−3.5	−6.2	0.0
Asp[231]					
SC (+)	4.3	6.2	7.0	8.1	5.0
SC (−)	−9.1	−11.4	−9.8	−13.0	−10.4
BB (+)	0.0	0.0	0.0	3.9	3.5
BB (−)	0.0	−4.6	−4.2	−5.1	−4.4
Arg[95]					
SC (+)	0.0	0.0	4.9	4.1	4.1
SC (−)	−3.8	−3.9	−5.4	−4.6	−4.3
Cys[105]					
SC (+)	3.2	4.6	5.5	4.4	4.5
SC (−)	−5.2	−5.8	−6.4	−5.1	−5.6
His[29]					
SC (+)	3.4	4.9	6.1	5.4	6.4
SC (−)	0.0	−4.8	−5.3	−5.9	−7.0
BB (+)	0.0	0.0	4.9	0.0	3.5
BB (−)	0.0	0.0	−3.2	0.0	0.0
Met[58]					
SC (+)	3.3	4.8	4.7	4.9	3.6
SC (−)	−5.5	−9.2	−9.0	−9.8	−7.3
Trp[99]					
SC (+)	0.0	3.5	3.8	0.0	0.0
SC (−)	0.0	−3.8	−4.2	0.0	0.0

Datasets	CW95K-ND3	CW95K-ND10	CW95K-ND30	Pulse-95K	Pulse-140K
S/D (e.A3/s)	0.006	0.012	0.016	0.009	0.016
Trp[201]					
SC (+)	3.6	3.2	6.1	4.1.	4.0
SC (−)	−3.9	−4.5	−6.1	−3.9	−5.4
Asn[168]					
SC (+)	3.3	3.2	4.4	3.2	3.5
SC (−)	−4.4	−3.4	−5.1	−4.2	−5.5
Water					
W4 (+)	0.0	0.0	5.6	0.0	0.0
W4 (−)	0.0	−3.9	−5.1	0.0	0.0
W7 (+)	0.0	5.0	3.0	4.1	0.0
W7 (−)	−4.1	−5.0	−5.8	−4.7	−4.7
Cl ion					
Cl-1 (−)	−9.8	−9.6	−11.3	−9.8	−8.7
Cl-1B (+)	4.9	5.1	5.1	4.1	4.7
Cl-3 (+)	3.6	3.4	0.0	0.0	0.0
Cl-4 (+)	0.0	3.8	7.6	0.0	4.9
Cl-5 (+)	3.8	4.5	4.6	4.2	3.8
Cl-6 (+)	4.0	4.6	6.7	5.3	3.4

early intermediate K states in the photocycle. In each case, the overall protein conformational change measured by global Cα shifts was very low. X-ray data for one study were released publicly, showing significant difference density only around the retinal, the water molecule hydrogen bonded to the chromophore becoming disordered, and Lys[216] moving sideways. Controversy arose once it was realized that the disorder of Asp[85] may be caused by radiation damage, since excessive exposure to x-rays can remove the carboxyl groups (28). Asp[85] and the conserved Asp[212] are the most sensitive residues, although the loss of these groups gives only negative difference density with no corresponding positive density. Care is therefore required to minimize x-ray exposure, especially if the same crystal is used to collect datasets in both the ground and excited states to reduce noise. bR is also known to show a color change on x-ray exposure, and difference Fourier maps show paired positive and negative peaks at the retinal and nearby water molecule. Matsui and colleagues (28) concluded that the changes due to x-ray exposure are significantly smaller than those of the K state in the photocycle. However, it is important to consider these effects in crystallographic studies of other rhodopsins, especially in regard to the earliest changes at the chromophore on photoexcitation. In this study, we used low temperature to block the photocycle of the chloride transporter NM-R3 at an early intermediate. To separate the effects of photoisomerization from those of x-ray damage, we used five separate crystals to determine independent difference Fourier maps showing the changes induced by different levels of photoexcitation. In this way, the effects of x-ray damage, which must be comparable for each dataset, may be distinguished from the effects of visible light.

Recently, structural changes in bR have been investigated through the use of XFELs to create time-resolved movies through a series of femtosecond snapshots (20), allowing comparison with previous crystallographic studies of trapped intermediates (29). XFEL allows the structural dynamics of retinal chromophore isomerization in bR to be studied at subpicosecond time scales (21), but the function of proton pumps remains extremely difficult to resolve because the hydrogen ion itself does not strongly scatter x-rays. Synchrotron radiation has now been used to study changes in bR over time scales from femtoseconds to milliseconds (29), but chloride ion transporters offer an enormous advantage over bR because the substrate is highly electron dense. Since proton and chloride pumps move their respective substrate ions in opposite directions and also have transporting mechanisms with different photocycles, it is necessary to study the structure of the light-induced active form of the chloride ion pump to understand its function. Previous studies of NpHR, which requires a homotrimeric conformation for activity, have documented light-induced structural changes under various conditions but did not detail the movement of chloride ions at high resolution (30). It was, however, found that removal of chloride from a site next to the chromophore leads to a large deformation of the C helix and the B-C loop (31). As with NM-R3, this chloride site overlays Asp[85] of bR.

In 2007, Gmelin and colleagues (32) described the x-ray structure of the L1 intermediate of hR, obtained by brief photostimulation at room temperature of a crystal subsequently cryo-cooled, giving a blue shift of the absorption band close to 580 nm. Since separate crystals were needed for each dataset, the difference maps had additional noise, and bromide was substituted for chloride to observe movements at two known binding sites; one halide ion close to the retinal was found to move only 0.3 Å, and the other, 14 Å closer to the external face of the protein, did not move measurably at all. Negative density close to the retinal was interpreted as isomerization, but no corresponding positive density was observed. Our study also shows the chloride ion close to the Schiff base moving very little
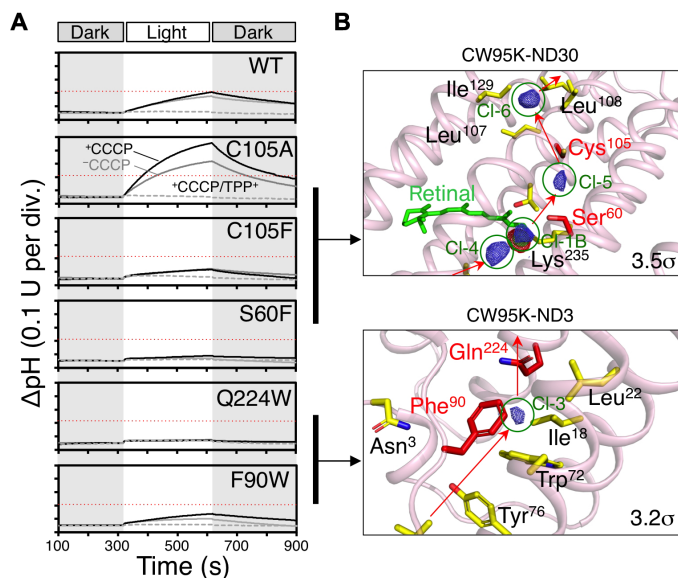
Fig. 4. Mutational analyses of functional residues in the chloride ion conduction pathway. (**A**) The anion-pumping activity of wild-type (WT) and mutant NM-R3 (C105A, C105F, S60F, Q224W, and F90W). Light-induced pH changes were measured using *Escherichia coli* cells expressing NM-R3 suspended in a solution containing 100 mM NaCl in the absence (gray solid lines) or presence (black solid lines) of the protonophore CCCP (30 μM) or in the presence of both 30 μM CCCP and 50 mM TPP[+] (black broken lines). The broken red line in each panel indicates the maximum activity level achieved by WT protein with photo-stimulation. div., division. (**B**) Positive difference electron density of CW95K-ND30 contoured at ±3.5σ (top) and CW95K-ND3 contoured at ±3.2σ (bottom), showing the path of chloride ions through the protein.

on constant photostimulation within NM-R3 crystals held at cryo-temperatures throughout, but other differences are noteworthy. In our study, we found density peaks within early intermediates of photoexcited NM-R3 that increased with stronger excitation and may be interpreted as waypoints on the path taken by chloride ions (movies S1 and S2). The changes at the chromophore are notably different, as well as from those observed in previous studies of bR (*19–21*), particularly the direction of movement and the fact that the lysine side chain moves more than the retinal itself. By comparing crystals subjected to different intensities of laser but an equal x-ray dose, this study provides definitive proof that the increased disorder of Asp[231] is not due to x-ray exposure and can be attributed to the effects of visible light. Since the light-minus-dark difference density maps depend only on the phases of the dark-state model (in which the retinal is clearly in the all-trans configuration), they are free of any bias that might be introduced by modeling the chromophore in an isomeric form in the photoexcited state. The absence of any significant difference density, despite the high resolution and quality of the diffraction data, shows that the retinal atoms move much less than might be expected. Retinal isomerization on light exposure is a much studied topic. Photoactivation of ATR free in solution produces a mixture of 9-cis, 11-cis, and 13-cis isomers, with a total yield of about 25%, but studies of bR show clearly that the rigid retinal pocket controls the isomerization, giving a much higher yield of about 67% of the 13-cis isomer (*33, 34*). It is known that mutation of Asp[85] or Asp[212] in bR greatly reduces the rate and products of the isomerization (*35, 36*), but the pocket of NM-R3 is substantially different, as described above. The hydrogen bond network formed by the side chains

of Ser[234], Tyr[204], Asp[231], and Arg[95] creates a rigid surface to one side of the PSB, with the chloride ion on the other, only 3.5 Å away from the nitrogen atom. The chloride ion is enclosed within the protein by a hydrogen bond between Ser[60] and Asn[98], equivalent to Ile[52] and Asp[85] in bR. Excitation of the retinal in bR involves charge transfer away from the PSB, which, in the case of NM-R3, would help the chloride ion move away, and sensory rhodopsins are known in which this effect rather than retinal isomerization triggers the protein (*37*). Further work is needed, in particular time-resolved studies by XFEL, to understand how energy captured by the chromophore is directed toward ion transport and the nature of later intermediates in the photocycle of the anion pump.

MATERIALS AND METHODS
Cloning, expression, and purification
The pET21b vector carrying the *NM-R3* gene derived from *Nonlabens marinus* was transformed into BL21-CodonPlus *Escherichia coli* (DE3; Agilent Technologies, Santa Clara, CA, USA). The cells were grown in a high-salt Luria-Bertani medium at 37°C. When cells reached an optical density at 600 nm (OD$_{600}$) of greater than 1.0, 50 μM ATR (Sigma-Aldrich, St. Louis, MO, USA) and 0.5 mM isopropyl-β-D-thiogalactopyranoside (IPTG) were added. NM-R3 was expressed for 6 to 8 hours at 30°C and harvested by ultracentrifugation at 3500*g* for 20 min at 4°C. Harvested cells were suspended in lysis buffer containing 50 mM tris-HCl (pH 7.0) and 150 mM NaCl and sonicated. The membrane fraction was isolated by ultracentrifugation at 370,000*g* for 40 min at 4°C and solubilized by incubating in resuspension buffer containing 50 mM tris-HCl (pH 7.0), 150 mM NaCl, 1% *n*-dodecyl-β-D-maltoside (DDM), and 0.2% cholesteryl hemisuccinate (CHS) for 2 hours at 4°C. Solubilized NM-R3 was purified by a TALON affinity column and then size exclusion chromatography (Superdex 200 16/60; GE Healthcare, Little Chalfont, UK) equilibrated with 20 mM Hepes (pH 7.5), 150 mM NaCl, 0.05% DDM, and 0.01% CHS. The eight NM-R3 mutants—C105A, C105F, S60F, Q224W, F90W, S234A, S234T, and S234N—were generated by site-directed mutagenesis and purified in the same manner.

Crystallization
Microcrystals suitable for conventional synchrotron experiments appeared in 0.15 M sodium chloride, 0.15 M calcium chloride, 0.1 M MES (pH 6.0), and 30% polyethylene glycol dimethyl ether 500 using NM-R3 at 45 mg/ml. Crystals grown in the lipidic cubic phase were harvested after 10 days. Crystals grew in space group *C2* and contained one monomer in the asymmetric unit (table S1).

Crystal illumination and structure determination
The crystals were illuminated by laser light under the same conditions as those used to measure each crystal absorption spectrum. The diffraction data were collected at beamline NW12A with a PILATUS3 S2M detector at the Photon Factory, KEK (Tsukuba, Japan). X-ray datasets were collected from each of the five separate crystals, i.e., in the dark (resting state) and treated with one of the irradiation protocols. The crystals diffracted to a resolution of at least 1.8 and 2.1 Å in the dark and photoexcited states, respectively. Total x-ray exposure time was under 10 min in the dark and light states at 95 or 140 K. All data were processed and scaled using HKL-2000 package (*38*) and CrysAlis[Pro] (Rigaku Oxford Diffraction, 2016). Initial models of the near-isomorphous light- and dark-state crystals were obtained by

molecular replacement with PHASER (*39*) using the previously solved NM-R3 structure [Protein Data Bank (PDB) 5G28]. The models were refined with a simulated-annealing protocol using a bulk solvent correction and further refined using Coot and PHENIX (*40, 41*). All data collection and refinement statistics are shown in table S1.

Calculation of difference Fourier density maps

Difference Fourier maps were generated using the CCP4 suite (*42*) and phenix.fobs_minus_fobs_map in PHENIX (*41*). Structure factor amplitudes were obtained using TRUNCATE, combined using CAD, and scaled using SCALEIT (*43, 44*). Last, difference Fourier electron density maps ($|F_{obs}|^{light} - |F_{obs}|^{dark}$)·exp.[$i\Phi^{calc}$] were calculated in fast Fourier transform using phases calculated from the refined dark-state structure (*45*).

Microspectrophotometry for single crystals

Light-induced absorption spectral changes in single crystals of NM-R3 were measured using a Nikon Eclipse TE2000-U inverted-type microscope equipped with a metal oxide semiconductor–type photodiode array (Unisoku PK-120). The NM-R3 single crystal on a cryo-loop was cooled to 95 or 140 K under a flow of cold nitrogen gas, and its absorption spectrum was measured before and during irradiation, either with a CW 532-nm laser diode module attenuated by 3, 10, or 30% ND filters (with final power densities of 1.1, 3.8, and 11 mW mm^{-2}, respectively) or with a 532-nm 10-kHz pulsed laser (FDSS532-Q2, CryLas, Berlin) with a 1% ND filter (with a final power density of ~0.47 mW mm^{-2}). A 532-nm notch filter (TECHSPEC OD6/25 mm, Edmund Optics) was used to minimize the effects of light scattering.

Measurement of NM-R3 activity

BL21-CodonPlus (DE3) *E. coli* cells expressing NM-R3 (wild type or mutant) were incubated at 37°C in high-salt Luria-Bertani medium supplemented with ampicillin (100 mg/ml). At an OD_{600} of 1.0, the overexpression of NM-R3 and mutants was induced by the addition of 1 mM IPTG and 50 μM ATR. Incubation was continued for 4 hours at 37°C. The cells were collected by centrifugation at 4000*g* for 5 min, washed four times with 100 mM NaCl buffer, and dissolved in the desired solvents, including CCCP (carbonyl cyanide 3-chlorophenylhydrazone) and TPP$^+$ (tetraphenylphosphonium chloride), until OD_{600} = 8.0. Cell suspensions were incubated in the dark for 2 hours before proton ion flux changes in the buffer were measured using an F-72G pH electrode (Horiba, Kyoto, Japan) under a 520-nm xenon light source (Elpisbio, Seoul, South Korea) at 25°C.

Ultraviolet-visible spectroscopy

Final samples were isolated in 10 mM Mops (pH 6.5) and 0.05% DDM using a Superdex 200 size exclusion column (GE Healthcare). The absorption spectra were scanned for samples (wild type, S234A, S234T, and S234N) using a V-650 spectrophotometer (JASCO, Oklahoma City, OK, USA) at 25°C. Anion titration experiments were performed by adding chloride ion, and SDs were calculated from triplicate experiments. Anion binding affinities were calculated using the Hill equation to analyze absorption changes at a wavelength of 581 nm, except in the case of S234A, for which data were measured at 596 nm. The dissociation constants are listed in fig. S8.

Difference distance matrix

The difference distance matrix of the light and dark forms of NM-R3 was calculated using the Differences Distance Matrix Program

(Center for Structural Biology, Yale University, New Haven, CT, USA). In the difference distance map, the changes in distance between Cα-Cα atoms were indicated by the brightness of the colors, and color saturation levels were set to represent Cα shifts of 0.5 Å closer (red) and 0.5 Å away (blue) (*46*).

Intensity quantification of difference Fourier map

Difference Fourier electron density maps ($|F_{obs}|^{light} - |F_{obs}|^{dark}$)·exp.[$i\Phi^{calc}$] were calculated for each crystal, and amino acid residues, water molecules, and chloride ions that show strong features in at least one of these maps are listed in Table 1. The root mean square electron density σ was determined by Coot, and values with a magnitude greater than ±3.0σ are indicated to one decimal place. Values below the threshold (3.0σ) are marked as zero (*20*).

REFERENCES AND NOTES

1. O. P. Ernst, D. T. Lodowski, M. Elstner, P. Hegemann, L. S. Brown, H. Kandori, Microbial and animal rhodopsins: Structures, functions, and molecular mechanisms. *Chem. Rev.* **114**, 126–163 (2014).
2. D. Oesterhelt, W. Stoeckenius, Rhodopsin-like protein from the purple membrane of halobacterium halobium. *Nat. New Biol.* **233**, 149–152 (1971).
3. B. Schobert, J. K. Lanyi, Halorhodopsin is a light-driven chloride pump. *J. Biol. Chem.* **257**, 10306–10313 (1982).
4. T. Kouyama, S. Kanada, Y. Takeguchi, A. Narusawa, M. Murakami, K. Ihara, Crystal structure of the light-driven chloride pump halorhodopsin from *Natronomonas pharaonis*. *J. Mol. Biol.* **396**, 564–579 (2010).
5. M. T. Facciotti, V. S. Cheung, D. Nguyen, S. Rouhani, R. M. Glaeser, Crystal structure of the bromide-bound D85S mutant of bacteriorhodopsin: Principles of ion pumping. *Biophys. J.* **85**, 451–458 (2003).
6. J. Sasaki, L. S. Brown, Y. S. Chon, H. Kandori, A. Maeda, R. Needleman, J. K. Lanyi, Conversion of bacteriorhodopsin into a chloride ion pump. *Science* **269**, 73–75 (1995).
7. O. Béjà, L. Aravind, E. V. Koonin, M. T. Suzuki, A. Hadd, L. P. Nguyen, S. B. Jovanovich, C. M. Gates, R. A. Feldman, J. L. Spudich, E. N. Spudich, E. F. DeLong, Bacterial rhodopsin: Evidence for a new type of phototrophy in the sea. *Science* **289**, 1902–1906 (2000).
8. H. Kandori, Ion-pumping microbial rhodopsins. *Front. Mol. Biosci.* **2**, 52 (2015).
9. K. Inoue, H. Ono, R. Abe-Yoshizumi, S. Yoshizawa, H. Ito, K. Kogure, H. Kandori, A light-driven sodium ion pump in marine bacteria. *Nat. Commun.* **4**, 1678 (2013).
10. K. Inoue, M. Konno, R. Abe-Yoshizumi, H. Kandori, The role of the NDQ motif in sodium-pumping rhodopsins. *Angew. Chem. Int. Ed. Engl.* **54**, 11536–11539 (2015).
11. T. Hosaka, S. Yoshizawa, Y. Nakajima, N. Ohsawa, M. Hato, E. F. DeLong, K. Kogure, S. Yokoyama, T. Kimura-Someya, W. Iwasaki, M. Shirouzu, Structural mechanism for light-driven transport by a new type of chloride ion pump, *Nonlabens marinus* rhodopsin-3. *J. Biol. Chem.* **291**, 17488–17495 (2016).
12. K. Kim, S.-K. Kwon, S.-H. Jun, J. S. Cha, H. Kim, W. Lee, J. F. Kim, H.-S. Cho, Crystal structure and functional characterization of a light-driven chloride pump having an NTQ motif. *Nat. Commun.* **7**, 12677 (2016).
13. H. E. Kato, K. Inoue, R. Abe-Yoshizumi, Y. Kato, H. Ono, M. Konno, S. Hososhima, T. Ishizuka, M. R. Hoque, H. Kunitomo, J. Ito, S. Yoshizawa, K. Yamashita, M. Takemoto, T. Nishizawa, R. Taniguchi, K. Kogure, A. D. Maturana, Y. Iino, H. Yawo, R. Ishitani, H. Kandori, O. Nureki, Structural basis for Na$^+$ transport mechanism by a light-driven na$^+$ pump. *Nature* **521**, 48–53 (2015).

14. M. Kolbe, H. Besir, L. O. Essen, D. Oesterhelt, Structure of the light-driven chloride pump halorhodopsin at 1.8 Å resolution. *Science* **288**, 1390–1396 (2000).

15. M. Schreiner, R. Schlesinger, J. Heberle, H. H. Niemann, Crystal structure of *Halobacterium salinarum* halorhodopsin with a partially depopulated primary chloride-binding site. *Acta Crystallogr. F Struct. Biol. Commun.* **72**, 692–699 (2016).

16. E. Krissinel, K. Henrick, Secondary-structure matching (SSM), a new tool for fast protein structure alignment in three dimensions. *Acta Crystallogr. D Biol. Crystallogr.* **60**, 2256–2268 (2004).

17. M. Sato, M. Kubo, T. Aizawa, N. Kamo, T. Kikukawa, K. Nitta, M. Demura, Role of putative anion-binding sites in cytoplasmic and extracellular channels of *Natronomonas pharaonis* halorhodopsin. *Biochemistry* **44**, 4775–4784 (2005).

18. T. Tsukamoto, S. Yoshizawa, T. Kikukawa, M. Demura, Y. Sudo, Implications for the light-driven chloride ion transport mechanism of *Nonlabens marinus* rhodopsin 3 by its photochemical characteristics. *J. Phys. Chem. B* **121**, 2027–2038 (2017).

19. K. Edman, P. Nollert, A. Royant, H. Belrhali, E. Pebay-Peyroula, J. Hajdu, R. Neutze, E. M. Landau, High-resolution x-ray structure of an early intermediate in the bacteriorhodopsin photocycle. *Nature* **401**, 822–826 (1999).

20. E. Nango, A. Royant, M. Kubo, T. Nakane, C. Wickstrand, T. Kimura, T. Tanaka, K. Tono, C. Song, R. Tanaka, T. Arima, A. Yamashita, J. Kobayashi, T. Hosaka, E. Mizohata, P. Nogly, M. Sugahara, D. Nam, T. Nomura, T. Shimamura, D. Im, T. Fujiwara, Y. Yamanaka, B. Jeon, T. Nishizawa, K. Oda, M. Fukuda, R. Andersson, P. Båth, R. Dods, J. Davidsson, S. Matsuoka, S. Kawatake, M. Murata, O. Nureki, S. Owada, T. Kameshima, T. Hatsui, Y. Joti, G. Schertler, M. Yabashi, A.-N. Bondar, J. Standfuss, R. Neutze, S. Iwata, A three-dimensional movie of structural changes in bacteriorhodopsin. *Science* **354**, 1552–1557 (2016).

21. P. Nogly, T. Weinert, D. James, S. Carbajo, D. Ozerov, A. Furrer, D. Gashi, V. Borin, P. Skopintsev, K. Jaeger, K. Nass, P. Båth, R. Bosman, J. Koglin, M. Seaberg, T. Lane, D. Kekilli, S. Brünle, T. Tanaka, W. Wu, C. Milne, T. White, A. Barty, U. Weierstall, V. Panneels, E. Nango, S. Iwata, M. Hunter, I. Schapiro, G. Schertler, R. Neutze, J. Standfuss, Retinal isomerization in bacteriorhodopsin captured by a femtosecond x-ray laser. *Science* **361**, eaat0094 (2018).

22. K. Inoue, F. H. Koua, Y. Kato, R. Abe-Yoshizumi, H. Kandori, Spectroscopic study of a light-driven chloride ion pump from marine bacteria. *J. Phys. Chem. B* **118**, 11190–11199 (2014).

23. M. T. Facciotti, S. Rouhani, F. T. Burkard, F. M. Betancourt, K. H. Downing, R. B. Rose, G. McDermott, R. M. Glaeser, Structure of an early intermediate in the M-state phase of the bacteriorhodopsin photocycle. *Biophys. J.* **81**, 3442–3455 (2001).

24. Y. Sudo, Y. Furutani, J. L. Spudich, H. Kandori, Early photocycle structural changes in a bacteriorhodopsin mutant engineered to transmit photosensory signals. *J. Biol. Chem.* **282**, 15550–15558 (2007).

25. K. Inoue, T. Tsukamoto, Y. Sudo, Molecular and evolutionary aspects of microbial sensory rhodopsins. *Biochim. Biophys. Acta* **1837**, 562–577 (2014).

26. W. Kühlbrandt, Bacteriorhodopsin—The movie. *Nature* **406**, 569–570 (2000).

27. C. Wickstrand, R. Dods, A. Royant, R. Neutze, Bacteriorhodopsin: Would the real structural intermediates please stand up? *Biochim. Biophys. Acta* **1850**, 536–553 (2015).

28. Y. Matsui, K. Sakai, M. Murakami, Y. Shiro, S.-i. Adachi, H. Okumura, T. Kouyama, Specific damage induced by x-ray radiation and structural changes in the primary photoreaction of bacteriorhodopsin. *J. Mol. Biol.* **324**, 469–481 (2002).

29. C. Wickstrand, P. Nogly, E. Nango, S. Iwata, J. Standfuss, R. Neutze, Bacteriorhodopsin: Structural insights revealed using x-ray lasers and synchrotron radiation. *Annu. Rev. Biochem.* **88**, 59–83 (2019).

30. T. Nakanishi, S. Kanada, M. Murakami, K. Ihara, T. Kouyama, Large deformation of helix F during the photoreaction cycle of *pharaonis* halorhodopsin in complex with azide. *Biophys. J.* **104**, 377–385 (2013).

31. S. Kanada, Y. Takeguchi, M. Murakami, K. Ihara, T. Kouyama, Crystal structures of an O-like blue form and an anion-free yellow form of *pharaonis* halorhodopsin. *J. Mol. Biol.* **413**, 162–176 (2011).

32. W. Gmelin, K. Zeth, R. Efremov, J. Heberle, J. Tittor, D. Oesterhelt, The crystal structure of the L1 intermediate of halorhodopsin at 1.9 Å resolution. *Photochem. Photobiol.* **83**, 369–377 (2007).

33. P. Hamm, M. Zurek, T. Röschinger, H. Patzelt, D. Oesterhelt, W. Zinth, Femtosecond spectroscopy of the photoisomerisation of the protonated Schiff base of all-trans retinal. *Chem. Phys. Lett.* **263**, 613–621 (1996).

34. K. A. Freedman, R. S. Becker, Comparative investigation of the photoisomerization of the protonated and unprotonated n-butylamine Schiff bases of 9-cis-, 11-cis-, 13-cis-, and all-trans-retinals. *J. Am. Chem. Soc.* **108**, 1245–1251 (1986).

35. L. Song, M. A. El-Sayed, J. K. Lanyi, Protein catalysis of the retinal subpicosecond photoisomerization in the primary process of bacteriorhodopsin photosynthesis. *Science* **261**, 891–894 (1993).

36. T. Yamato, T. Kakitani, Molecular dynamics simulation of the excited-state dynamics of bacteriorhodopsin. *Photochem. Photobiol.* **66**, 735–740 (1997).

37. K. W. Foster, J. Saranak, F. Derguini, G. R. Zarrilli, R. Johnson, M. Okabe, K. Nakanishi, Activation of chlamydomonas rhodopsin in vivo does not require isomerization of retinal. *Biochemistry* **28**, 819–824 (1989).

38. Z. Otwinowski, W. Minor, Processing of x-ray diffraction data collected in oscillation mode. *Methods Enzymol.* **276**, 307–326 (1997).

39. A. J. McCoy, R. W. Grosse-Kunstleve, P. D. Adams, M. D. Winn, L. C. Storoni, R. J. Read, Phaser crystallographic software. *J. Appl. Crystallogr.* **40**, 658–674 (2007).

40. P. Emsley, K. Cowtan, Coot: Model-building tools for molecular graphics. *Acta Crystallogr. D Biol. Crystallogr.* **60**, 2126–2132 (2004).

41. P. D. Adams, P. V. Afonine, G. Bunkóczi, V. B. Chen, I. W. Davis, N. Echols, J. J. Headd, L.-W. Hung, G. J. Kapral, R. W. Grosse-Kunstleve, A. J. McCoy, N. W. Moriarty, R. Oeffner, R. J. Read, D. C. Richardson, J. S. Richardson, T. C. Terwilliger, P. H. Zwart, Phenix: A comprehensive python-based system for macromolecular structure solution. *Acta Crystallogr. D Biol. Crystallogr.* **66**, 213–221 (2010).

42. Collaborative Computational Project, Number 4, The CCP4 suite: Programs for protein crystallography. *Acta Crystallogr. D Biol. Crystallogr.* **50**, 760–763 (1994).

43. P. H. Zwart, Anomalous signal indicators in protein crystallography. *Acta Crystallogr. D Biol. Crystallogr.* **61**, 1437–1448 (2005).

44. P. L. Howell, G. D. Smith, Identification of heavy-atom derivatives by normal probability methods. *J. Appl. Cryst.* **25**, 81–86 (1992).

45. R. J. Read, A. J. Schierbeek, A phased translation function. *J. Appl. Cryst.* **21**, 490–495 (1988).

46. R. M. Richards, C. E. Kundrot, Identification of structural motifs from protein coordinate data: Secondary structure and first-level supersecondary structure. *Proteins* **3**, 71–84 (1988).